

Supporting Information

3D Printed Nickel-Molybdenum-Based Electrocatalysts for Hydrogen Evolution at Low Overpotentials in a Flow-Through Configuration

Ian Sullivan¹, Huanlei Zhang³, Cheng Zhu², Marissa Wood², Art J. Nelson², Sarah E. Baker²,
Christopher M. Spadaccini², Tony Van Buuren², Meng Lin^{3*}, Eric B. Duoss^{2*}, Siwei Liang^{2*},
and Chengxiang Xiang^{1*}

¹ *Joint Center for Artificial Photosynthesis, and Department of Applied Physics and Material Science, California Institute of Technology, Pasadena, California 91125, United States*

² *Lawrence Livermore National Laboratory, 7000 East Avenue, Livermore, CA 94550, USA*

³ *Department of Mechanical and Energy Engineering, Southern University of Science and Technology, Shenzhen, Guangdong 518055, China*

Corresponding Authors

Email: cxx@caltech.edu*, liang11@llnl.gov*, duoss1@llnl.gov*, linm@sustech.edu.cn*

Methods

Synthesis of 3D Printing Resin: A resorcinol-based polymer precursor was prepared by following the procedure reported by Liu et al.¹ The Ni-Mo inks were prepared by mixing MoCl_5 , $\text{NiNO}_3 \cdot 6\text{H}_2\text{O}$, block-copolymer binder Pluronic 127, resorcinol-based polymer precursor and deionized water in appropriate mass ratios. The precursors were then mixed by a planetary centrifugal mixer (Thinky) for 5 min at 2500 RPM to afford a homogeneous and clear ink. The Ni-Mo ink was loaded into a syringe barrel (EFD) attached by a Luer-Lock to a smooth-flow tapered nozzle (200 μm inner diameter, d). The pressure to extrude the ink through the nozzle was controlled by an air-powered fluid dispenser (Ultimus V, EFD). The targeted 3D patterns were printed using an x-y-z 3-axis air bearing positioning stage (ABL 9000, Aerotech), whose motion was controlled by the appropriate G-code commands. The 3D NiMo structures were printed onto arbitrary slides and immersed into dodecane immediately after printing and allowing them gel at 80 °C. The diameter of the cylindrical rods was controlled by the diameter of nozzle (d), and the center-to-center rod spacing (L) was varied in a range of 400 to 100 μm . After gelation, the 3D parts were removed from the slide surface and washed briefly with acetone before freeze-drying. NiMo inks were printed in a lattice configuration in a 2.4 cm x 2.4 cm area with successive layers printed directly on top. Electrodes were printed with a standard 32-layer thickness, resulting in an average thickness of 4 mm.

Electrode Fabrication: 3D printed NiMo substrates were cut to ~5 mm x 5 mm pieces and thoroughly rinsed with deionized water and dried under vacuum for 12 hours at 60 °C. A length of enamel coated copper wire was cut, and the ends were shaved with a razor to expose the conductive Cu metal. Conductive Ag epoxy (Ted Pella) was used to adhere the Cu wire to the edge of the NiMo substrate and allowed to dry in air for ~30 minutes. Epoxy (Loctite, EA 9640) was then applied to cover the dried Ag epoxy and Cu wire, leaving only NiMo exposed to the electrolyte (Figure S2). The NiMo electrodes were then positioned at the end of a quartz tube and epoxied at the edges, allowing for electrolyte to flow through the face of the electrode (Figure S2).

Hydrogen Evolution: Hydrogen evolution reaction (HER) was performed in an H-cell with cathode and anode compartments separated using an anion exchange membrane (AEM). A three-electrode configuration was employed with NiMo as the working electrode, Pt coil as the counter electrode, and a Ag/AgCl reference electrode (eDAQ). The electrolyte was purged with 100 sccm dry N₂ 1 hour prior to, and during all electrochemical measurements. Electrolyte flow rate was controlled by a peristaltic pump and recirculated in the cathode compartment of the cell.

Materials Characterization: A scanning electron microscope (SEM, FEI Inc., NOVA NanoSEM 450) with an integrated energy-dispersive X-ray (EDX) spectrometer was used to analyze the morphology and elemental composition, respectively. Images were taken using an accelerating voltage of 15 kV. EDX images were taken with an accelerating voltage of 15 kV.

X-ray diffraction (XRD) measurements were taken with a Bruker D8 Discover X-ray diffractometer using Cu K α radiation (1.54056 Å) in Bragg-Brentano geometry. Diffraction images were collected using a two-dimensional VÅNTEC-500 detector and integrated into one-dimensional patterns using DIFFRAC.SUITE™ EVA software.

X-ray photoelectron spectroscopy (XPS) was performed on a PHI Quantum 2000 system using a focused monochromatic Al Ka x-ray (1486.7 eV) source for excitation and a spherical section analyzer. The instrument has a 16-element multichannel detection system. A 200 um diameter X-ray beam was used for analysis. The X-ray beam is incident normal to the sample and the X-ray detector is at 45° away from the normal. The pass energy was 23.5 eV giving an energy resolution of 0.3 eV that when combined with the 0.85 eV full width at half maximum (FWHM) Al Ka line width gives a resolvable XPS peak width of 1.2 eV FWHM. Deconvolution of non-resolved peaks was accomplished using Multipak 9.6.1A (PHI) curve fitting routines. The collected data were referenced to an energy scale with binding energies for Cu 2p_{3/2} at 932.72± 0.05 eV and Au 4f_{7/2} at 84.01± 0.05 eV. Binding energies were also referenced to the C 1s photoelectron line arising from adventitious carbon at 284.8 eV. XPS core-level analysis in combination with ion beam sputtering (1 kV Ar⁺, 1 x 1 mm) was performed to determine composition and bonding versus depth. The sputter rate is ~ 13.5 nm/min.

XPS compositional analysis was accomplished by measuring the integrated XPS peak area and dividing by the respective atomic sensitivity factor and thus obtaining the atomic percent concentration with an accuracy of ±0.1%.

Electrochemical Measurements: Electrochemical measurements were performed in a custom two-compartment H cell using a Biologic SP-300 model potentiostat. The NiMo electrode served as a working electrode and Ag/AgCl (eDAQ) as a reference electrode in the same compartment. In a separate compartment, a Pt coil was used as the counter electrode. Both compartments were separated by an anion exchange membrane (FAA-3-50, Fumatech). All measurements were performed at room temperature (25 °C) and pressure (1 atm). The working compartment was purged with research grade 5 N₂ (99.999% purity, Airgas) for 60 min prior to, and during the experiments.

Electrochemical Impedance Spectroscopy: EIS measurements were taken using a range of frequencies of 200 kHz to 0.1 Hz and an amplitude of 10 mV. Data were fit using the ZFit software (Bio-Logic).

Electrochemical Surface Area Measurements: Double layer capacitance (C_{DL}) measurements were performed by cyclic voltammetry scans in a range ±50 mV from open circuit voltage (OCV). The potential at each vertex was held for 10 s before scanning in the other direction. Scan rates ranged from 1, 2, 5, 10, 20, 50 and 100 mVs⁻¹. C_{DL} is proportional to the electrochemical surface area (ECSA) and is given by the equation

$$i_c = \nu C_{dl}$$

Where i_c is the charging current (mA), and ν is the scan rate (V/s). Charging current was plotted as a function of scan rate, with the slope equal to C_{dl} (mF). The ECSA (cm²) was then calculated using the equation

$$ECSA = \frac{C_{dl}}{C_s}$$

Where C_s is the electrolyte dependent solution capacitance (mF cm^{-2}). We chose to assume a C_s value of 0.04 mF cm^{-2} as previously described.^{2,3}

Roughness factor (RF) is defined by

$$RF = \frac{ECSA}{A_{geo}}$$

Where A_{geo} is the geometrical area (cm^2) of the electrode.

Electrode Area Measurement: The geometrical area of the electrode was measured using the ImageJ software program (National Institutes of Health). This software package has the ability to convert pixels to distance and can also measure area. A high-resolution picture of the electrode was taken in the same plane as a ruler, and a known linear distance was measured in the program to convert pixels to cm. The electrode area perimeter was then highlighted, and the area was integrated.

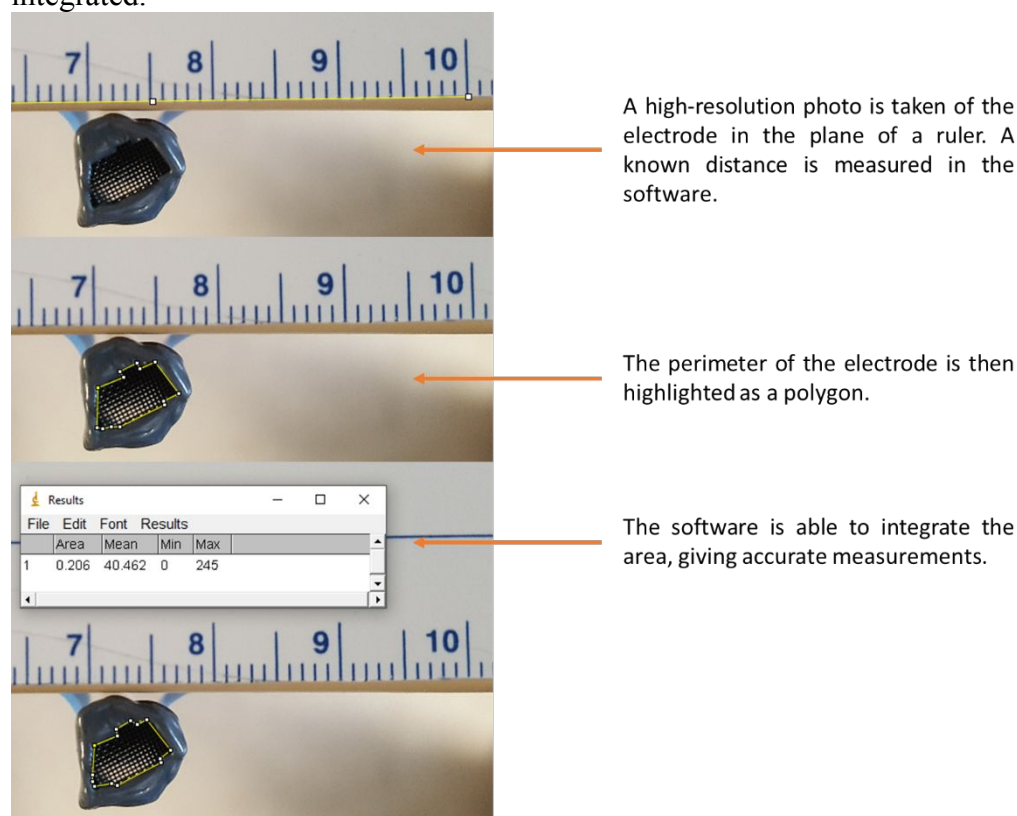


Figure S1. Electrode 2D surface area measurements using ImageJ software

3D Surface Area Estimation: The 3D surface area was estimated by assuming the flow-through channels of the electrode were rectangular in shape, were consistent through the entire electrode, and were unobstructed through the thickness of the electrode. We used the following schematic to determine the inner surface area of the channels, as well as the surface area of the carbon fiber faces.

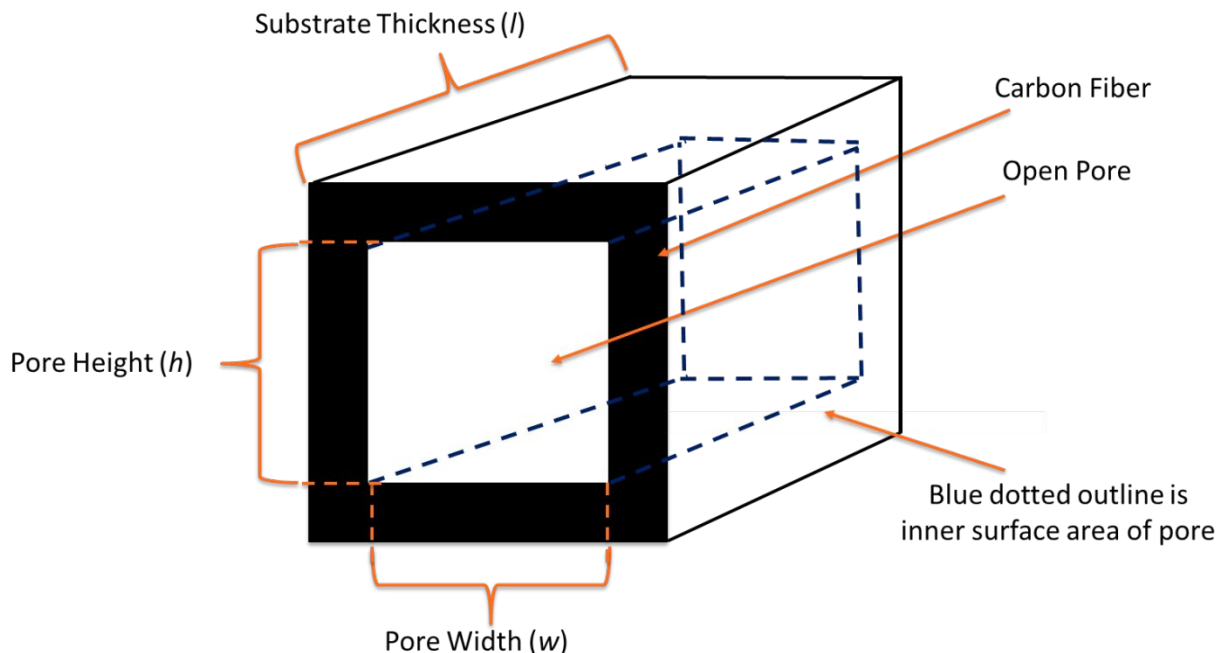


Figure S2. Estimation of 3D geometric area for flow-through electrodes.

SEM images were used to measure the pore dimensions as well as the carbon fiber thickness. The inner surface area was calculated using the formula

$$3D \text{ Geometric Area} = 2(wl + hl) * n$$

Where w is the width of the pore (cm) measured by SEM, h is the length of the pore (cm) measured by SEM, and l is the substrate thickness (cm) measured with calipers. This value was then multiplied by the total number of exposed pores (n) of the electrode to obtain the total estimated 3D geometric area.

Gas Product Analysis: H_2 was measured with online gas chromatography (GC, customized SRI instruments Model 8610C) every 3 min. A thermal conductivity detector (TCD) was used to detect H_2 using a Molsieve 5\AA column for H_2 , O_2 , and N_2 separation. An isothermal method was used with an oven temperature of $110\text{ }^\circ\text{C}$, TCD temperature of $105\text{ }^\circ\text{C}$, and injection valve temperature of $60\text{ }^\circ\text{C}$. Research grade 5 Ar carrier gas was set to 20 psi.

Electrochemical Surface Roughening: NiMo electrodes were immersed in 1.0 M KOH electrolyte and 10 cyclic voltammetry (CV) cycles were performed ranging from -1.0 V to 1.5 V , at a scan rate of 10 mVs^{-1} . After scanning, the electrode was rinsed with deionized water and dried under a N_2 stream.

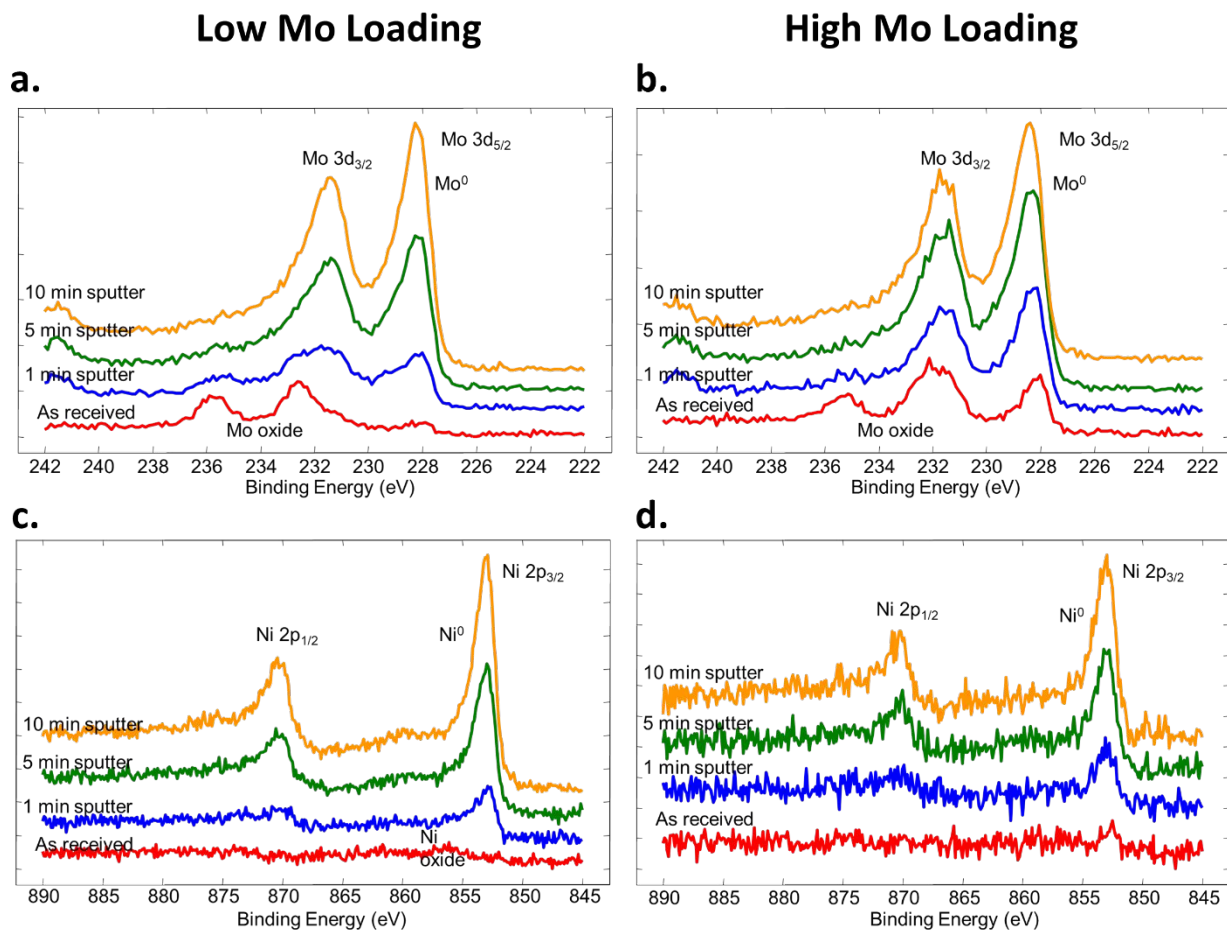


Figure S3. Mo 3d spectra from XPS measurements for 0.68 wt. % Mo (a), and 3.03 wt. % Mo (b) electrodes. Ni 2p spectra for 0.68 wt. % Mo (c), and 3.03 wt. % Mo (d) electrodes.

Table S1. Atomic compositions for 0.68 wt. % Mo electrodes from XPS measurements

<u>Sample</u>	<u>Mo (at. %)</u>	<u>Ni (at. %)</u>	<u>C (at. %)</u>	<u>O (at. %)</u>
As Received	0.65	0.72	94.04	4.59
1 min Sputter	1.07	1.2	94.11	3.62
5 min Sputter	2.06	3.12	91.74	3.08
10 min Sputter	3.16	4.76	90.36	1.72

Table S2. Atomic compositions for 3.03 wt. % Mo electrodes from XPS measurements

<u>Sample</u>	<u>Mo (at. %)</u>	<u>Ni (at. %)</u>	<u>C (at. %)</u>	<u>O (at. %)</u>
As Received	1.36	0.91	92.99	4.74
1 min Sputter	2.36	1.39	93.38	2.87
5 min Sputter	4.10	5.45	88.89	1.56
10 min Sputter	4.75	3.6	90.09	1.56

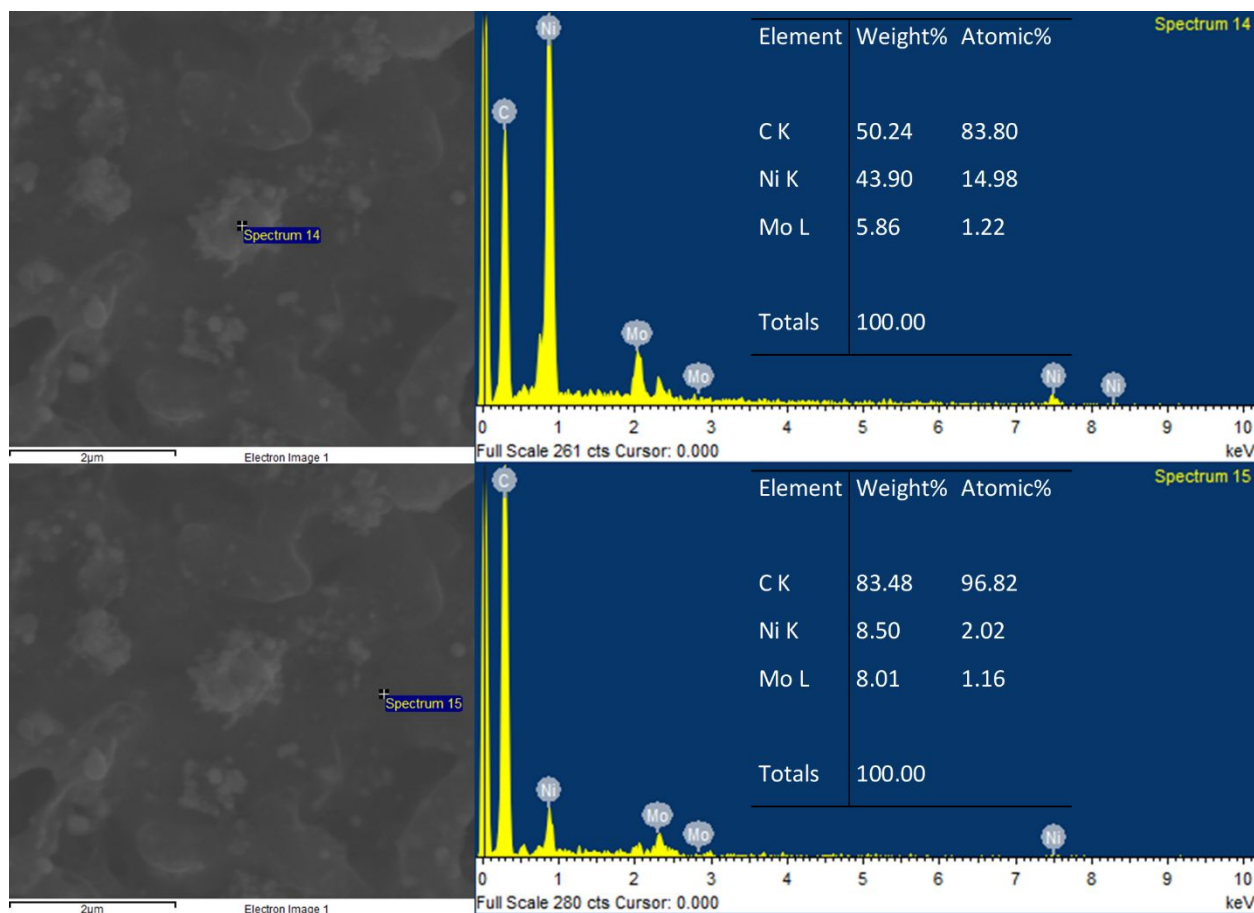


Figure S4. Point spectra from EDX measurements. The spectrum shows a larger Ni contribution at the nodule (top) then compared to the darker region (bottom).

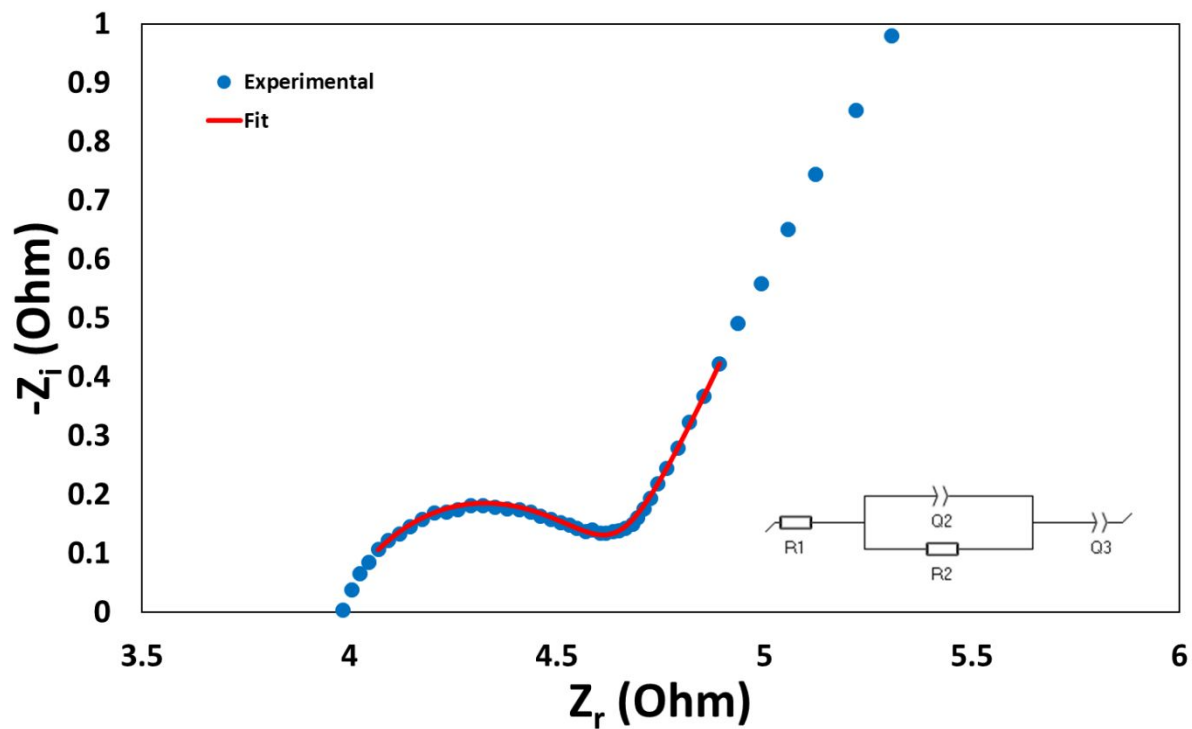


Figure S5. Representative electrochemical impedance spectroscopy (EIS) curves for NiMo flow-through electrodes. Inset: Model circuit used to fit the data.

Table S3. R_s and R_{ct} values for varying Mo content electrodes

<u>Material</u>	<u>Mo Wt. %</u>	<u>R_s</u>	<u>R_{CT}</u>
NiMo Lo	0.68	3.963	0.6777
NiMo Mid	1.88	2.909	0.8269
NiMo Hi	3.03	6.08	0.3062

Table S4. Overpotentials from C, oxidized C, and NiMo electrodes

Material	η 10 mA cm⁻² (mV)	Mo Wt. %	RF
C	524	0	435
C (Oxidized)	361	0	2166
NiMo Lo	134	0.68	26122
NiMo Mid	103.6	1.88	23059
NiMo Hi	68.2	3.03	25753
NiMo (Flat, No Spacing)	209	3.03	13024

Table S5. Overpotentials and RFs for various NiMo electrodes

Mo Wt. %	Log RF	Overpotential (mV)
0.681	4.792	97.36
1.389	3.750	265
1.883	4.657	130.6
2.397	4.712	112.4
3.034	4.745	103.6

Table S6. Cited References Using ECSA or RF as Figures of Merit for Electrocatalytic Performance

Electrocatalytic Reaction	Electrode	ECSA (cm²)	RF	C_{DL} (mF cm⁻²)	Reference
CO ₂ Reduction	Porous Ag/Al Foam	172	422	N/A	4
CO Reduction	Cu on Porous Carbon	970	3167	N/A	5
Oxygen Evolution	Carbon Doped NiO	N/A	N/A	111.9	6
Hydrogen Evolution	MoS ₂ -Carbon	N/A	N/A	2.53	7
	Ni	N/A	N/A	2.99	8

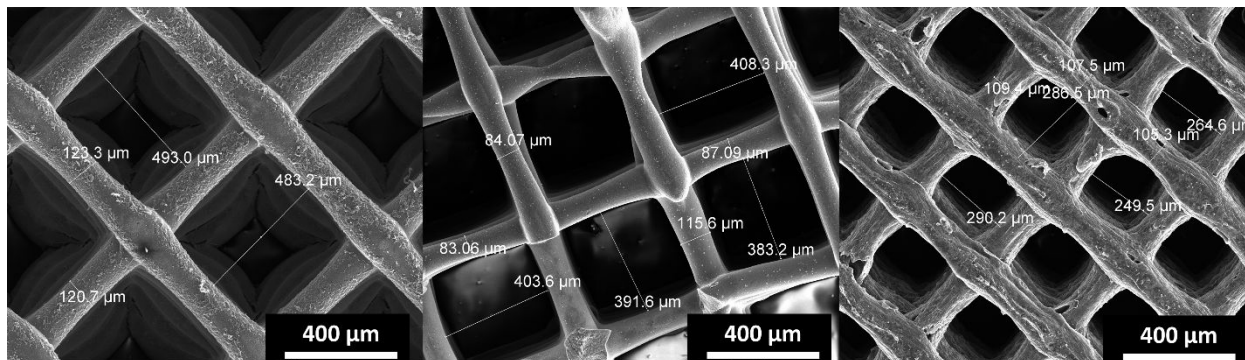


Figure S6. SEM images of NiMo electrodes 3D printed with varying pore sizes.

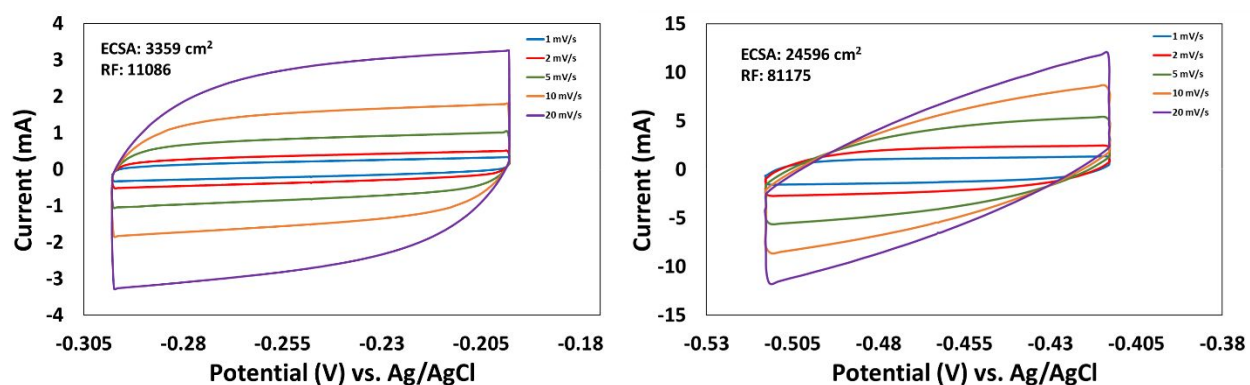


Figure S7. ECSA measurements for NiMo electrodes before (left) and after (right) electrochemical surface roughening.

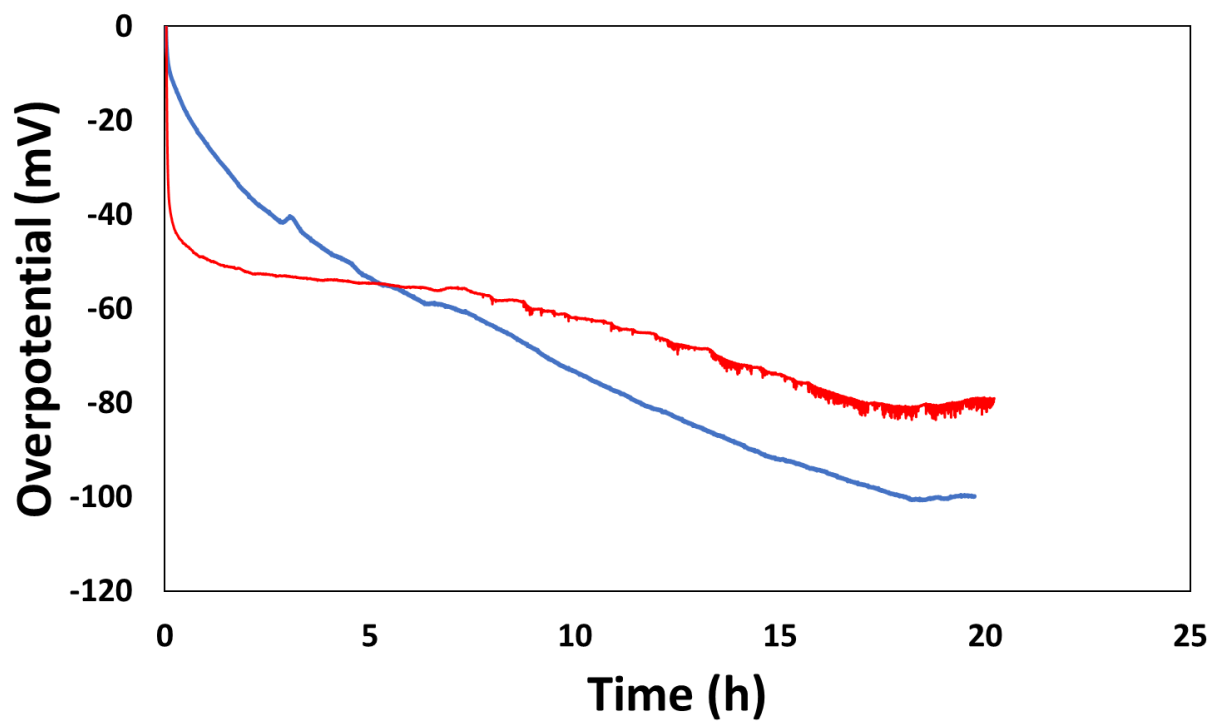


Figure S8. Chronopotentiometric measurements of 3D printed NiMo at 10 mA cm^{-2} before (blue) and after (red) oxidation treatments.

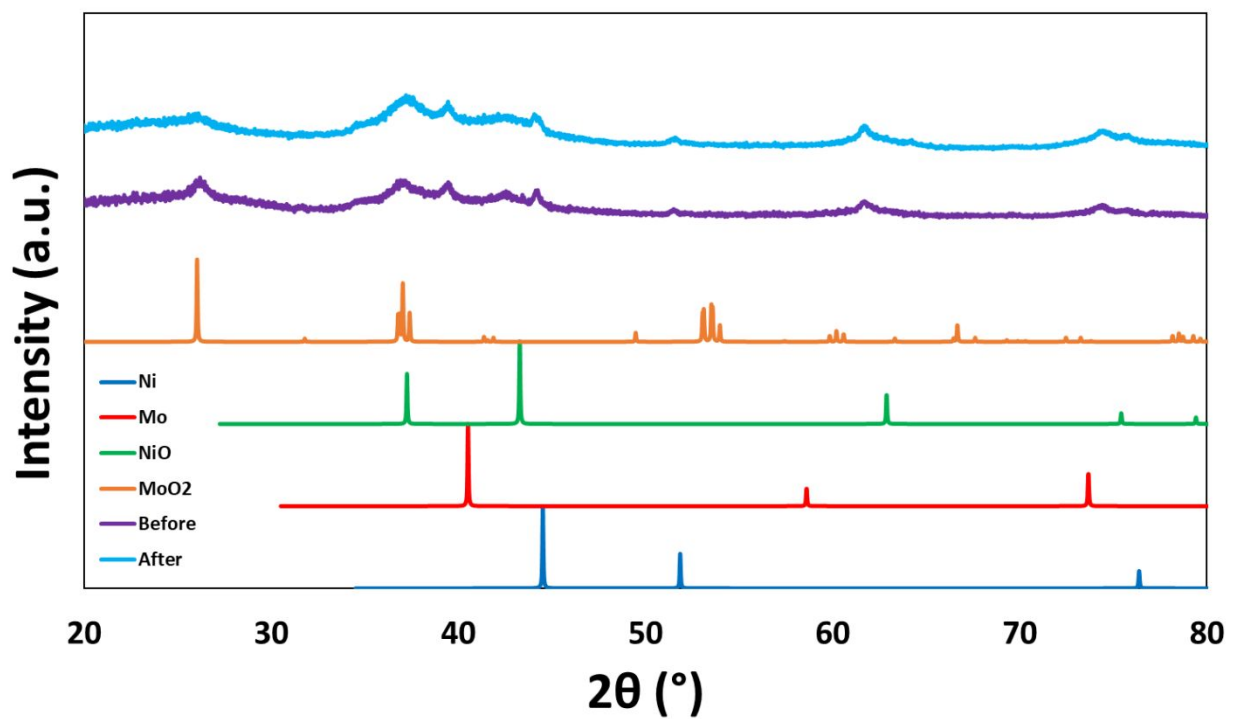


Figure S9. XRD patterns of 3.03 Wt. % Mo content NiMo before and after oxidation and HER measurements.

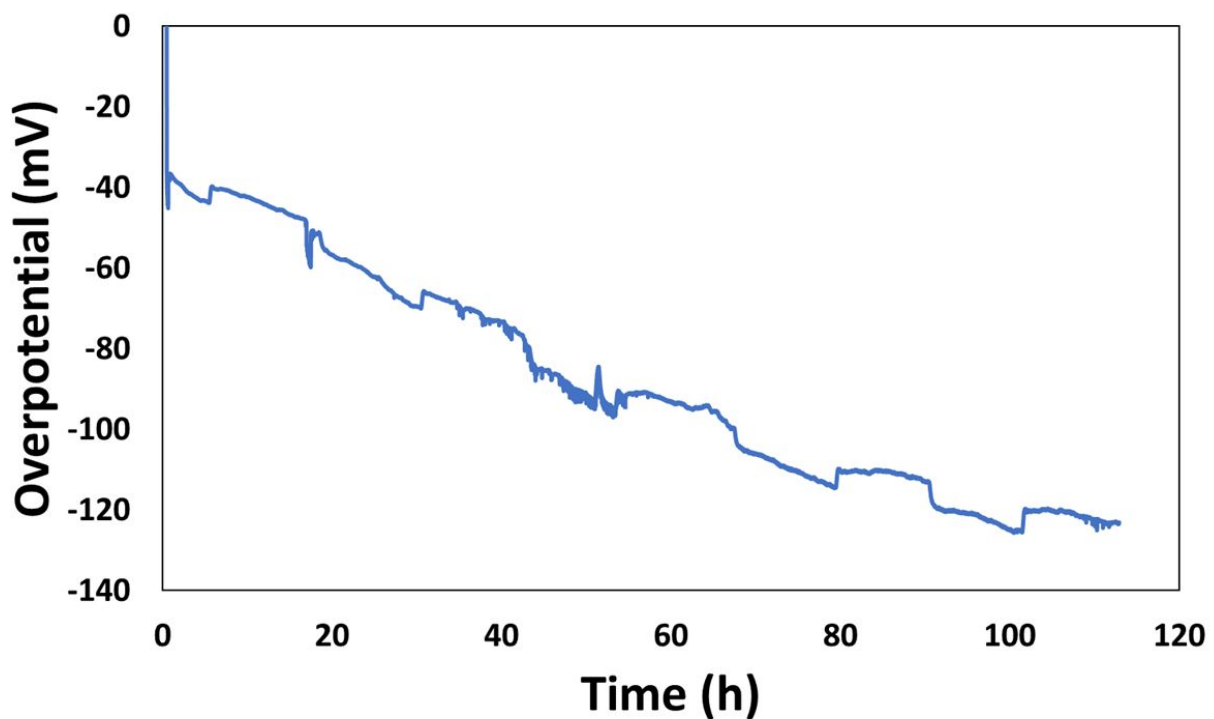


Figure S10. Long-term electrolysis for HER at 10 mA cm⁻² using oxidized high Mo content NiMo electrode.

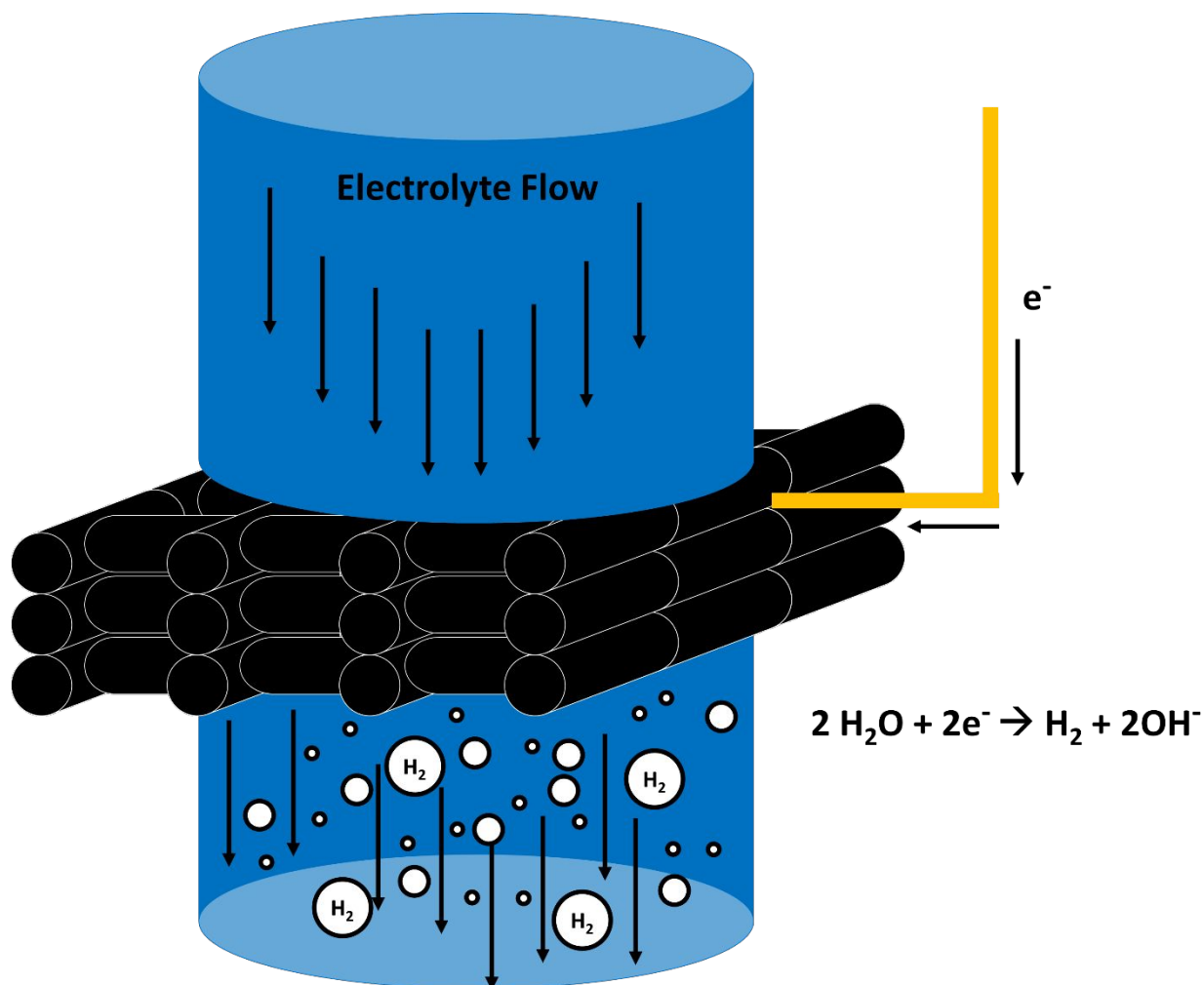


Figure S11. Schematic of the flow-through configuration for NiMo-based electrodes.

References

- (1) Liu, R.; Shi, Y.; Wan, Y.; Meng, Y.; Zhang, F.; Gu, D.; Chen, Z.; Tu, B.; Zhao, D. Triconstituent Co-Assembly to Ordered Mesostructured Polymer-Silica and Carbon-Silica Nanocomposites and Large-Pore Mesoporous Carbons with High Surface Areas. *J. Am. Chem. Soc.* **2006**, *128* (35), 11652–11662. <https://doi.org/10.1021/ja0633518>.
- (2) McCrory, C. C. L.; Jung, S.; Peters, J. C.; Jaramillo, T. F. Benchmarking Heterogeneous Electrocatalysts for the Oxygen Evolution Reaction. *J. Am. Chem. Soc.* **2013**, *135* (45), 16977–16987. <https://doi.org/10.1021/ja407115p>.
- (3) McCrory, C. C. L.; Jung, S.; Ferrer, I. M.; Chatman, S. M.; Peters, J. C.; Jaramillo, T. F. Benchmarking Hydrogen Evolving Reaction and Oxygen Evolving Reaction Electrocatalysts for Solar Water Splitting Devices. *J. Am. Chem. Soc.* **2015**, *137* (13), 4347–4357. <https://doi.org/10.1021/ja510442p>.
- (4) Vedharathinam, V.; Qi, Z.; Horwood, C.; Bourcier, B.; Stadermann, M.; Biener, J.; Biener, M. Using a 3D Porous Flow-Through Electrode Geometry for High-Rate

- Electrochemical Reduction of CO₂ to CO in Ionic Liquid. *ACS Catal.* **2019**, *9* (12), 10605–10611. <https://doi.org/10.1021/acscatal.9b03201>.
- (5) Han, L.; Zhou, W.; Xiang, C. High-Rate Electrochemical Reduction of Carbon Monoxide to Ethylene Using Cu-Nanoparticle-Based Gas Diffusion Electrodes. *ACS Energy Lett.* **2018**, *3* (4), 855–860. <https://doi.org/10.1021/acseenergylett.8b00164>.
- (6) Kou, T.; Wang, S.; Shi, R.; Zhang, T.; Chiovoloni, S.; Lu, J. Q.; Chen, W.; Worsley, M. A.; Wood, B. C.; Baker, S. E.; et al. Periodic Porous 3D Electrodes Mitigate Gas Bubble Traffic during Alkaline Water Electrolysis at High Current Densities. *Adv. Energy Mater.* **2020**, *2002955*, 1–11. <https://doi.org/10.1002/aenm.202002955>.
- (7) Murthy, A. P.; Theerthagiri, J.; Madhavan, J.; Murugan, K. Highly Active MoS₂/Carbon Electrocatalysts for the Hydrogen Evolution Reaction – Insight into the Effect of the Internal Resistance and Roughness Factor on the Tafel Slope. *Phys. Chem. Chem. Phys.* **2017**, *19* (3), 1988–1998. <https://doi.org/10.1039/C6CP07416B>.
- (8) Herraiz-Cardona, I.; Ortega, E.; Antón, J. G.; Pérez-Herranz, V. Assessment of the Roughness Factor Effect and the Intrinsic Catalytic Activity for Hydrogen Evolution Reaction on Ni-Based Electrodeposits. *Int. J. Hydrogen Energy* **2011**, *36* (16), 9428–9438. <https://doi.org/10.1016/j.ijhydene.2011.05.047>.